

Efficient variational contraction of two-dimensional tensor networks with a non-trivial unit cell

A. Nietner^{1,2}, B. Vanhecke³, F. Verstraete³, J. Eisert^{1,2}, and L. Vanderstraeten³

¹Dahlem Center for Complex Quantum Systems, Freie Universität Berlin, D-14195 Berlin, Germany

²Helmholtz-Zentrum Berlin für Materialien und Energie, 14109 Berlin, Germany

³Department of Physics and Astronomy, University of Ghent, Krijgslaan 281, 9000 Gent, Belgium

2020-04-29

Tensor network states provide an efficient class of states that faithfully capture strongly correlated quantum models and systems in classical statistical mechanics. While tensor networks can now be seen as becoming standard tools in the description of such complex many-body systems, close to optimal variational principles based on such states are less obvious to come by. In this work, we generalize a recently proposed variational uniform matrix product state algorithm for capturing one-dimensional quantum lattices in the thermodynamic limit, to the study of regular two-dimensional tensor networks with a non-trivial unit cell. A key property of the algorithm is a computational effort that scales linearly rather than exponentially in the size of the unit cell. We demonstrate the performance of our approach on the computation of the classical partition functions of the antiferromagnetic Ising model and interacting dimers on the square lattice, as well as of a quantum doped resonating valence bond state.

1 Introduction

Tensor network methods are increasingly becoming a standard tool for studying the physics of strongly-correlated systems, both from the perspective of a theoretical and mathematical understanding of many-body effects as well as for providing a versatile toolbox for numerical simulations[1–6]. In the context of one-dimensional quantum physics, *matrix product states (MPS)* have been identified to parametrize the low-energy states of gapped local Hamiltonians, in fact provably so. MPS-based algorithms allow for efficient simulations of static and dynamic properties of spin chains in various facets [7] and allow for precise numerical analysis of symmetry protected topological order in one dimension [8–10]. Two-dimensional quantum systems can be simulated using instances of *projected entangled-pair states (PEPS)*. Indeed, the

A. Nietner: anietner@physik.fu-berlin.de

B. Vanhecke: bavhecke.vanhecke@ugent.be

PEPS toolbox is increasingly capturing ground state [11–14], dynamic [15–17], spectral [18, 19], and finite-temperature [20, 21], properties as well as the simulation of open system dynamics [22] of quantum spins or electrons in two dimensions. In the field of classical statistical mechanics, tensor networks provide a natural way of simulating e.g. critical and/or frustrated systems in two [23] and three [24, 25] dimensions, which are notoriously difficult for standard sampling methods.

When applying tensor networks to two- and three-dimensional systems, both quantum and classical, the computational bottleneck always consists of the contraction of a two-dimensional tensor network. In the easiest case, one considers a translation-invariant tensor network on a regular lattice in the thermodynamic limit, i.e. the network consists of a single tensor that is repeated over an infinite lattice. In the past, different algorithms have been proposed for this fundamental task, which can be subdivided into three main approaches: (i) Real-space renormalization-group methods [26–31] rely on coarse-graining transformations on the level of the tensors that make up the network, such that global properties of the tensor network can be efficiently computed. (ii) In corner transfer matrix methods [32–37], part of the network is represented by effective corner tensors which are obtained by an iterative growing of the environment and truncation of the tensors. (iii) Boundary methods aim to approximate the fixed point of the row-to-row transfer matrix as an MPS, such that this MPS represents an effective representation of half of the network; different algorithms can be used to find the fixed point such as the density-matrix renormalization group [1, 23], the time-evolving block decimation [38, 39], the tensor ring decomposition [40, 41] or the VUMPS algorithm [42–44].

The two former approaches rely on power methods to find a fixed point for the contraction of an infinite tensor network, whereas the latter two iterate local self-consistency relations. In particular variational MPS-tangent-space methods such as VUMPS can exploit more advanced solvers for the leading eigenvector of the transfer matrix. This property leads to a significant speed-up for the VUMPS algorithm as

compared to power methods when critical or close-to-critical tensor networks are considered [42, 45].

In many applications, the relevant two-dimensional tensor network cannot be chosen to be translation invariant, but rather consists of a larger unit cell of different tensors that are repeated over the infinite lattice. In other scenarios, the tensor network itself is translation-invariant but the lattice symmetry is spontaneously broken. In both cases, an algorithm with uniform tensors can not be used for the contraction. Whereas corner transfer matrix approaches have been extended to the case of larger unit cells [12, 46], the variational boundary-MPS methods have not been formulated in this more general setting. In this work, we show that this generalization of the VUMPS algorithm is, in fact, a very natural one and leads to an algorithm with a complexity that scales linearly with the size of the non-trivial unit cell.

2 Set-up

In this section we review the basic ingredients that allow for the contraction of translation-invariant two-dimensional tensor networks using the VUMPS algorithm [42], setting the stage for the multi-site version in the next section.

2.1 Two-dimensional tensor networks

Two-dimensional tensor networks are most naturally obtained in the context of two-dimensional statistical mechanics, where they appear as a representation of the partition function of lattice spin models with local interactions. Indeed, suppose we have a system of spins $s_i = \pm 1$ on a regular, say square, lattice with nearest-neighbour interactions

$$\mathcal{H} = \sum_{\langle i,j \rangle} H(s_i, s_j). \quad (1)$$

The partition function for this model is given by

$$\begin{aligned} \mathcal{Z} &= \lim_N \sum_{s \in \{\pm 1\}^N} e^{-\beta \mathcal{H}(s)} \\ &= \lim_N \sum_{s \in \{\pm 1\}^N} \prod_{\langle i,j \rangle} e^{-\beta H(s_i, s_j)}. \end{aligned} \quad (2)$$

We can now write this partition function as a tensor network by placing a local Boltzmann weight represented by the symmetric matrix t

$$\text{---} \textcircled{t} \text{---} = e^{-\beta H(s_1, s_2)} \quad (3)$$

on each link on the lattice, placing a δ tensor

$$c \text{---} \textcircled{\delta} \text{---} a = \begin{cases} 1, & a = b = c = d \\ 0, & \text{else} \end{cases}, \quad (4)$$

on each site, and contracting all connected indices. In this way, we arrive at

$$\mathcal{Z} = \dots \begin{array}{ccc} \vdots & \vdots & \vdots \\ \text{---} \textcircled{M} \text{---} & \textcircled{M} & \text{---} \textcircled{M} \text{---} \\ \vdots & \vdots & \vdots \\ \text{---} \textcircled{M} \text{---} & \textcircled{M} & \text{---} \textcircled{M} \text{---} \\ \vdots & \vdots & \vdots \\ \text{---} \textcircled{M} \text{---} & \textcircled{M} & \text{---} \textcircled{M} \text{---} \\ \vdots & \vdots & \vdots \end{array} \dots \quad (5)$$

with

$$\textcircled{M} = \begin{array}{c} \text{---} \textcircled{q} \text{---} \\ | \\ \text{---} \textcircled{q} \text{---} \\ | \\ \text{---} \textcircled{q} \text{---} \\ | \\ \text{---} \textcircled{q} \text{---} \end{array} \quad (6)$$

where $q^2 = t$. A local expectation value of an observable O with values O_j , $j = \pm 1$, at site i is given by changing one tensor in this tensor network, i.e.,

$$\langle O^i \rangle = \frac{1}{\mathcal{Z}} \dots \begin{array}{ccc} \vdots & \vdots & \vdots \\ \text{---} \textcircled{M} \text{---} & \textcircled{N} & \text{---} \textcircled{M} \text{---} \\ \vdots & \vdots & \vdots \\ \text{---} \textcircled{M} \text{---} & \textcircled{N} & \text{---} \textcircled{M} \text{---} \\ \vdots & \vdots & \vdots \\ \text{---} \textcircled{M} \text{---} & \textcircled{N} & \text{---} \textcircled{M} \text{---} \\ \vdots & \vdots & \vdots \end{array} \dots \quad (7)$$

where the new tensor N is given by

$$\textcircled{N} = \begin{array}{c} \text{---} \textcircled{q} \text{---} \\ | \\ \text{---} \textcircled{q} \text{---} \\ | \\ \text{---} \textcircled{q} \text{---} \\ | \\ \text{---} \textcircled{q} \text{---} \\ | \\ \text{---} \textcircled{O} \text{---} \end{array} \quad (8)$$

and is placed at site i . Similarly one can represent generic n -point functions by placing the n defect tensors in the form of Eq. (8) at the corresponding sites in the partition function Eq. (5).

Two-dimensional tensor networks also show up as the norm or local expectation values of two-dimensional PEPS. Then, the elementary four leg tensor M is given as the sandwich of the PEPS tensor and its conjugate

$$\begin{array}{c} (a, \bar{a}) \\ | \\ \textcircled{M} \\ | \\ (d, \bar{d}) \end{array} \text{---} (b, \bar{b}) = \begin{array}{c} a \\ | \\ \textcircled{} \\ | \\ \bar{a} \end{array} \text{---} \begin{array}{c} b \\ | \\ \textcircled{} \\ | \\ \bar{b} \end{array} \quad (9)$$

where the thick leg on the left hand side corresponds to the tensor product of the two thin legs of the respective side of the PEPS tensor.

To contract two dimensional tensor networks it is natural to use the fact that topological two dimensional systems (trivial or non-trivial) are in general

gives rise to gauging errors ϵ_L and ϵ_R as

$$\epsilon_L = \left\| \left| \begin{array}{c} \text{---} A_L \text{---} \\ \text{---} A_C \text{---} \\ \text{---} A_L \text{---} \end{array} \right. \right\|_2 \quad (20)$$

and

$$\epsilon_R = \left\| \left| \begin{array}{c} \text{---} A_C \text{---} \\ \text{---} C \text{---} \\ \text{---} A_R \text{---} \end{array} \right. \right\|_2. \quad (21)$$

2.4 Variational optimization for uniform matrix product states (VUMPS)

The VUMPS algorithm [42] is a fixed point iteration method for finding the boundary of a two-dimensional tensor network. The desired fixed point equation is obtained starting from expressing the eigenvalue equation for the boundary state Eq. (10) in terms of MPS as

$$\begin{array}{c} \text{---} A_L \text{---} \\ \text{---} A_C \text{---} \\ \text{---} A_R \text{---} \\ \text{---} M \text{---} \\ \text{---} M \text{---} \\ \text{---} M \text{---} \end{array} \approx \lambda \begin{array}{c} \text{---} A_L \text{---} \\ \text{---} A_C \text{---} \\ \text{---} A_R \text{---} \end{array}. \quad (22)$$

The approximation sign in Eq. (22) is due to the MPS approximation of the boundary, and signifies that we aim at finding an MPS that approximates this equation in an optimal way. Here, we chose the following optimality condition: We interpret the set of MPS with a given bond dimension χ as a variational manifold \mathcal{M}_χ . Next, we observe that the MPS on the left hand side of Eq. (22) has bond dimension χD , with D the bond dimension of the MPO, whereas the MPS on the right hand side has bond dimension χ . Then, optimality with respect to the variational manifold \mathcal{M}_χ implies that the left hand side variationally truncated to χ should equal the right hand side. This optimality condition can be reformulated as saying that we look for the MPS for which the error made in Eq. (22) is orthogonal (in Hilbert space) to the tangent space on the manifold. Put differently, the tangent space projector of the manifold applied to the equation should vanish to guarantee the optimal solution within the variational manifold.

The tangent space projector \mathcal{P}_A at A (projecting any state in the many body Hilbert space onto its overlap with the tangent space at the state parametrized by A) can be graphically written as [43]

$$\begin{aligned} \mathcal{P}_A = & \sum_{i \in \mathbb{Z}} \left(\begin{array}{c} \text{---} A_L \text{---} \\ \text{---} A_L \text{---} \end{array} \right) \left| \begin{array}{c} \text{---} A_R \text{---} \\ \text{---} A_R \text{---} \end{array} \right. - \left. \begin{array}{c} \text{---} A_L \text{---} \\ \text{---} A_L \text{---} \end{array} \right| \begin{array}{c} \text{---} A_R \text{---} \\ \text{---} A_R \text{---} \end{array} \right) \\ = & \sum_{i \in \mathbb{Z}} \left(\begin{array}{c} \text{---} A_L \text{---} \\ \text{---} A_L \text{---} \end{array} \right) \left| \begin{array}{c} \text{---} A_R \text{---} \\ \text{---} A_R \text{---} \end{array} \right. - \left. \begin{array}{c} \text{---} A_L \text{---} \\ \text{---} A_L \text{---} \end{array} \right| \begin{array}{c} \text{---} A_R \text{---} \\ \text{---} A_R \text{---} \end{array} \right) \end{aligned} \quad (23)$$

where i denotes the site in the lattice at which the picture is centred. Introducing the tensors

$$\frac{1}{\mathcal{N}} \begin{array}{c} \text{---} A_L \text{---} \\ \text{---} A_C \text{---} \\ \text{---} A_R \text{---} \\ \text{---} M \text{---} \\ \text{---} M \text{---} \\ \text{---} M \text{---} \end{array} = \begin{array}{c} \text{---} A_C \text{---} \end{array} \quad (24)$$

and

$$\frac{1}{\mathcal{N}'} \begin{array}{c} \text{---} A_L \text{---} \\ \text{---} A_L \text{---} \\ \text{---} C \text{---} \\ \text{---} A_R \text{---} \\ \text{---} M \text{---} \\ \text{---} M \text{---} \\ \text{---} M \text{---} \end{array} = \begin{array}{c} \text{---} C \text{---} \end{array} \quad (25)$$

where the diverging \mathcal{N} and \mathcal{N}' denote the normalizations counteracting the non-normalized tensors M , one finds [42] that the vanishing of the tangent space projector on Eq. (22) is equivalent to Eq. (13) together with

$$\begin{array}{c} \text{---} A_C \text{---} \end{array} = \begin{array}{c} \text{---} A_L \text{---} \\ \text{---} C \text{---} \end{array} = \begin{array}{c} \text{---} C \text{---} \\ \text{---} A_R \text{---} \end{array}. \quad (26)$$

Moreover, because the gauge transformation C transforming A_L and A_R into each other is unique up to a factor, it must hold that $A'_C \propto A_C$. This leads to the VUMPS equations

$$\frac{1}{\mathcal{N}} \begin{array}{c} \text{---} A_L \text{---} \\ \text{---} A_C \text{---} \\ \text{---} A_R \text{---} \\ \text{---} M \text{---} \\ \text{---} M \text{---} \\ \text{---} M \text{---} \end{array} = \tau_{A_C} \begin{array}{c} \text{---} A_C \text{---} \end{array} \quad (27)$$

and

$$\frac{1}{\mathcal{N}'} \begin{array}{c} \text{---} A_L \text{---} \\ \text{---} A_L \text{---} \\ \text{---} C \text{---} \\ \text{---} A_R \text{---} \\ \text{---} M \text{---} \\ \text{---} M \text{---} \\ \text{---} M \text{---} \end{array} = \tau_C \begin{array}{c} \text{---} C \text{---} \end{array}. \quad (28)$$

Together with Eq. (13), Eq. (27) and (28) fully characterize the fixed point. To solve this equation we run into one obvious problem: The isometries A_L and A_R are not known unless we have identified the full MPS, which we do not know if we want to solve for $|\psi(A)\rangle$. Still, we can use the framework from above to iteratively approximate the desired fixed point.

Starting from a random MPS and solving this equation once for A_C and C respectively we can use Eq. (14) and (15) to find a new MPS approximating this pair of tensors with a gauging error $\max\{\epsilon_L, \epsilon_R\}$. This update implicitly defines a non-linear map in the MPS manifold. Iterating the procedure we will eventually converge to the fixed point of this map represented by a pair of A_C and C with vanishing gauging

and

$$\frac{1}{\mathcal{N}'} \dots = \tau_C \cdot C \dots \quad (45)$$

A more detailed derivation of these fixed-point equations can be found in Appendix B. The variational optimality can be easily understood as shown in Appendix A.2.

3.3 The algorithm

We obtain the n_y coupled local equations for the A_C and C tensors Eq. (44) and (45) which, together with Eq. (33) and (35) implicitly defines a flow through the coupled MPS manifolds of the n_y boundaries. This flow can be integrated just as in 2.4. To do so we solve the local equations Eq. (44) and (45) for an initial set of MPS, update all boundaries according to the just obtained solutions for A_C and C using Eq. (33) and (35). Again, derive the new local equations according to the current set of boundaries. Iterate this procedure until convergence is reached.

Let us now phrase this in explicit algorithmic form. We can compute the left and right channels in (44) and (45) explicitly by using the leading left and right eigenvectors of the transfer matrices respectively. To this end, we can either use (40) for the consecutive application of the transfer matrices. However, Eq. (46) and Eq. (47) are already optimal in complexity because we are dealing with matrices rather than MPOs. On the other hand, for sufficiently small gaps γ_i in the transfer matrices (cf. Eq (39)) Eq (40) leads to more stability. Moreover, using an iterative solver we can exploit the tensor-network structure to reduce the memory allocation. Thus one obtains a computational effort of $\mathcal{O}(D^2\chi^3 + D^4\chi^2)$ compared to $\mathcal{O}(D^2\chi^4)$, which can further be reduced by parallelizing². The equation for the $n_y \times n_x$ left eigenvectors is

$$\dots = \alpha_{x,y}^L \cdot L \dots \quad (46)$$

where we have drawn the dependence of the tensors on x and y explicitly for the sake of clarity. The dots imply the matrix product over the n_x transfer matrices

²In terms of the PEPS bond dimension D_P those complexities correspond to $\mathcal{O}(D_P^4\chi^3 + D_P^8\chi^2)$ compared to $\mathcal{O}(D_P^4\chi^4)$.

contained in one unit cell of the y -th row. Similarly, the equations for the right eigenvectors are

$$\dots = \alpha_{x,y}^R \cdot R \dots \quad (47)$$

Note, while we need to solve this equation for all y we can fix the x value and obtain the remaining environment tensors via applying the respective transfer matrices (followed by a normalization).

We can now use the (x, y) -dependent environments $(L_{x,y})_{x,y}$ and $(R_{x,y})_{x,y}$ in order to define the application of the local fixed point equations h_{A_C} and h_C corresponding to (44) and (45) that we will use to iteratively solve for the tensors A_C and C

$$\dots = \lambda_{A_C} \cdot A_C \dots \quad (48)$$

and

$$\dots = \lambda_C \cdot C \dots \quad (49)$$

Let us recapitulate the algorithm: To start we initialize a set of n_y MPS with a unit cell of size n_x , each of these MPS corresponding to a boundary. Then we derive the local equations h_{A_C} (cf. (48)) and h_C (cf. (49)) using (46) and (47). Solving h_{A_C} and h_C we obtain new tensors A_C for all x and y and C for all x and y . Using these we update the boundaries using (33) and (35) obtaining a gauging error. To do so, use either (33) or (35) to get a set of left (right) canonical tensors from the A_C and C together with the respective gauging errors. Next find the right (left) canonical representation of these tensors as in Ref. [44] Algorithm 2. The left and right canonical tensors define the boundaries for the next iteration. Next, start again from the beginning until the gauging error is smaller than a desired threshold ϵ . The algorithm is shown with more structure in Algorithms 1 and 2. Note, instead of using the gauging error one might as well use the singular values of the C tensors as convergence criterion. Finally, instead of the parallel update just defined one could as well use a sequential update in the x direction (cf. Appendix C).

Algorithm 1: Explicit terms of the local Hamiltonians in the parallel implementation.

Function `environment_terms`(($M_{x,y}$) $_{x,y}$, ($A_L^{x,y}$) $_{x,y}$, ($A_R^{x,y}$) $_{x,y}$, ϵ):

- $(L_{x,y})_{x,y} \leftarrow$ compute left eigenvector according to (46)
- $(R_{x,y})_{x,y} \leftarrow$ compute left eigenvector according to (47)
- return** ($L_{x,y}$) $_{x,y}$ and ($R_{x,y}$) $_{x,y}$

Function `apply_h_a_c`(($A_C^{x,y}$) $_{x,y}$):

- $(A_C^{x,y})_{x,y} \leftarrow$ update according to (48)
- return** ($A_C^{x,y}$) $_{x,y}$

Function `apply_h_c`(($C^{x,y}$) $_{x,y}$):

- $(C^{x,y})_{x,y} \leftarrow$ update according to (49)
- return** (C^y) $_y$

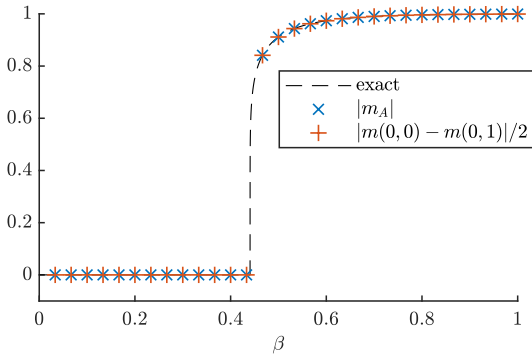


Figure 1: Different measures of the magnetization of the anti-ferromagnetic Ising model in the unit cell in the absence of a magnetic field compared to exact results (dashed line) for $\chi = 20$. Absolute value of the magnetization at site (0,0) (crosses) and half distance of magnetization between neighbouring sites (pluses).

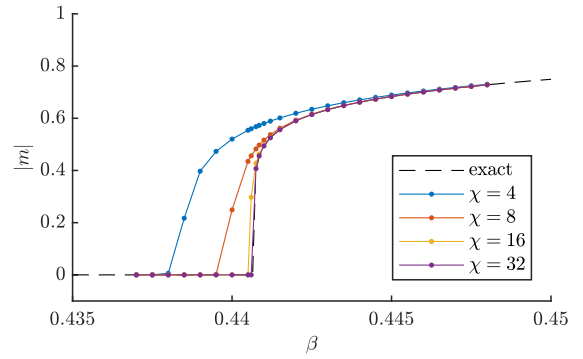


Figure 2: Zoom in to the phase transition between the disordered and ordered phase for various values of $\chi = 4, 8, 16$ and 32 highlighting the bond dimension dependence of the accuracy of the algorithm. Notably, for higher bond dimensions the difference between the numerical and exact results around the critical point is no longer visible in the present resolution.

4 Test cases and benchmarks

4.1 Classical anti-ferromagnetic Ising model

To test the multi-site VUMPS algorithm we investigate the classical anti-ferromagnetic Ising model on a square lattice with a magnetic field. This is given by the partition function

$$\mathcal{Z}(\beta, J, h, N) = \sum_{s \in \{\pm 1\}^{\times N}} \exp(-\beta \mathcal{H}(s, J, h)), \quad (50)$$

$$\mathcal{H}(s, J, h) = J \sum_{\langle i, j \rangle} s_i s_j + h \sum_i s_i, \quad (51)$$

where $\langle i, j \rangle$ denotes the sum over nearest neighbours on the square lattice. We can write this partition function as a two-dimensional tensor network on the square lattice from the tensor

$$\text{---} \bigcirc \text{---} = \begin{array}{c} \text{---} \bigcirc \text{---} \\ | \\ \text{---} \bigcirc \text{---} \\ | \\ \text{---} \bigcirc \text{---} \\ | \\ \text{---} \bigcirc \text{---} \end{array} \quad (52)$$

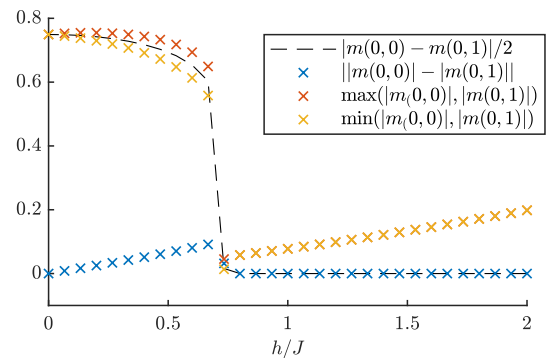


Figure 3: Magnetic phase transition at $\beta = 0.45$ from the anti-ferromagnetic phase to the magnetically ordered ferromagnetic phase. Various measures are shown such as the half distance of the magnetization between neighbouring sites (dashed line), distance of absolute values of magnetizations between neighbouring sites (blue crosses), maximum (red crosses) and minimum (yellow crosses) of the absolute values of the magnetization at sites (0,0) and (0,1), respectively.

Algorithm 2: Parallel implementation of the VUMPS algorithm for non-trivial unit cells.

Data: MPO $M = (M_{x,y})_{x,y}$ with (n_x, n_y) shaped unit cell; desired accuracy ϵ_{prec}

Result: Array containing the data of n_y MPS corresponding to the boundaries $(|\psi(A_y)\rangle\rangle_y)$

```

 $(|\psi(A_y)\rangle\rangle_y \leftarrow$  initialize MPS array
 $(L_{x,y})_{x,y}, (R_{x,y})_{x,y} \leftarrow$  update environments from  $\{(|\psi(A_y)\rangle\rangle_y, M)\}$  calling environment_terms
 $\epsilon_{trunc} \leftarrow 1$ 
 $(\epsilon_{trunc,y})_y \leftarrow (1)_y$ 
while  $\epsilon_{trunc} > \epsilon_{prec}$  do
   $(A_C^{x,y})_{x,y} \leftarrow$  solve  $h_{AC}$  using an iterative solver calling apply_h_a_c
   $(C^{x,y})_{x,y} \leftarrow$  solve  $h_C$  using an iterative solver calling apply_h_c
  for  $y \in \{0, \dots, n_y\}$  do
     $\{A_{L/R}^{x,y}\}_x, \epsilon_{trunc,y} \leftarrow \{(A_C^{x,y})_x, (C^{x,y})_x\}$  following (33) or (35)
     $|\psi(A_y)\rangle\rangle \leftarrow \{A_{L/R}^{x,y}\}_x$  by finding the mixed gauge (similar to Algorithm 2 in Ref. [44])
   $\epsilon_{gauge} \leftarrow \max\{\epsilon_{gauge,y}\}$ 
   $(L_{x,y})_{x,y}, (R_{x,y})_{x,y} \leftarrow$  update environments from  $\{(|\psi(A_y)\rangle\rangle_y, M)\}$  calling environment_terms

```

where

$$\text{---} \textcircled{q} \textcircled{q} \text{---} = \begin{pmatrix} e^{-\beta J} & e^{\beta J} \\ e^{\beta J} & e^{-\beta J} \end{pmatrix} \quad (53)$$

and

$$\textcircled{h} \text{---} = \begin{pmatrix} e^{\beta h} \\ e^{-\beta h} \end{pmatrix}. \quad (54)$$

Although the partition function of the Ising anti-ferromagnet can be represented by a single tensor M , it actually has a non-trivial unit cell. This can be easily seen as follows. The partition function of the anti-ferromagnet equals that of the Ising ferromagnet after a sub-lattice rotation flipping every second spin in the lattice. This transformation has a 2×2 unit cell. Also, this sub-lattice rotation would map a homogenous magnetic field to a staggered magnetic field highlighting this unit cell. This actually reflects the fact that the anti-ferromagnetic partition function has a vanishing norm if restricted to odd lattices. Hence, the thermodynamic limit is only well defined if restricting to even lattices. This behaviour can be nicely observed using our algorithm. So in a sense, the anti-ferromagnet is a ferromagnet with a non-trivial unit cell.

Fixing $J = 1$ we can map the physics of Eq. (50) into the plane spanned by $\beta \geq 0$ and $h \in \mathbb{R}$. For $h = 0$ we can compute the magnetization within the unit cell and compare to exact results. As for $h = 0$ the anti-ferromagnet equals the ferromagnet with every second site flipped in the z basis, we expect a staggered magnetization in the unit cell with the same strength as for the ferromagnet. In Fig. 1 we show our results obtained with algorithm 4 for bond dimension $\chi = 20$. We compare the absolute value of the magnetization of the first site in the unit cell $(x, y) = (0, 0)$ with the exact results. Moreover, we compare to the half distance between consecutive sites in the unit cell

$|m(0, 0) - m(0, 1)|/2$ where $m(x, y)$ is the magnetization at the unit cell site (x, y) . We find perfect agreement for all quantities up to machine precision.

We have investigated the phase transition around $\beta_c \approx 0.44068$ in more detail in Fig. 2. We have computed $|m(0, 0)|$ for various bond dimensions $\chi = 12, 16, 20, 28, 36, 44$. Only very close to the critical point our results start to deviate from the exact values depending on the bond dimension, reflecting the fact that low- χ MPS cannot describe critical states accurately. In order to further illustrate our results, in Fig. 4 we show the magnetization in the unit cell depending on β for $h = 0$. One can nicely see the emergence of the staggered magnetization through the phase transition.

Next, we have investigated the transition from a staggered magnetized phase to an ordered magnetized phase at $\beta = 0.45$ and along $h \in [0, 2]$. In Fig. 3 we show our results for various quantities obtained from the local magnetizations $m(x, y)$. One can nicely see the linear dependence of the difference between the absolute values of the local magnetizations of consecutive sites until the phase transition around $h_c(\beta = 0.45) \approx 0.74$, where it drops to zero and the local magnetizations start to point in the same direction with the same values. In Fig. 5 we have visualized this process by plotting the local magnetizations in the unit cell for four consecutive values of h at $\beta = 0.45$, nicely showing the transition from an anti-ferromagnetic to a ferromagnetic order.

4.2 Interacting dimers on the square lattice

As a second benchmark, we consider a model of interacting dimers on the square lattice [54, 55]. This model starts from the well-known dimer-counting problem, which was solved exactly in the early sixties [56–58]. This problem can be extended to a statis-

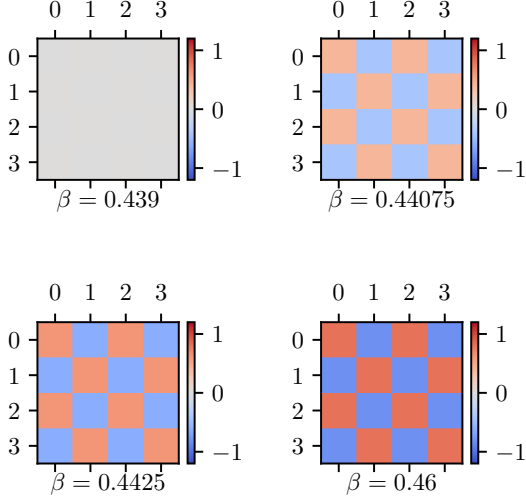


Figure 4: Heatmap visualizing the emergence of the anti-ferromagnetic order within the unit cell through the thermal phase transition $\beta = 0.439$ (top left), $\beta = 0.44075$ (top right), $\beta = 0.4425$ (bottom left), $\beta = 0.46$ (bottom right) for $\chi = 44$.

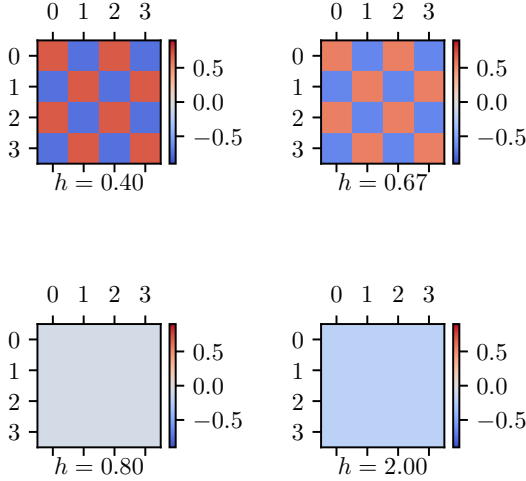


Figure 5: Heatmap visualizing the magnetization within the unit cell through the magnetic phase transition for magnetic fields $h = 0.4$ (top left), $h = 0.6667$ (top right), $h = 0.8$ (bottom left) and $h = 2$ (bottom right) at $\chi = 20$.

tical mechanics model, where the allowed configurations are determined by all dimer coverings and we can associate an energy to each dimer configuration. A natural choice for the energy E_c of a given configuration is the number of parallel dimers,

$$E_c = - \sum_p N_p(c), \quad (55)$$

where the sum is over all plaquettes and $N_p(c)$ is either one or zero (depending on whether there are two parallel dimers on plaquette p for the configuration c). We include a minus sign in order to favour parallel dimer configurations. The partition function is obtained by summing the Boltzmann weights over all configurations

$$\mathcal{Z} = \sum_c e^{\beta \sum_p N_p(c)}. \quad (56)$$

with $\beta = 1/T$ the inverse temperature. This model has been shown [54, 55] to exhibit rotational and translational symmetry breaking in a so-called columnar phase, quantified by the order parameter

$$D = \frac{1}{\mathcal{Z}} \sum_c e^{\beta \sum_p N_p(c)} \frac{1}{N} \left(\sum_{l \in \mathcal{V}} M_l(c) - \sum_{l \in \mathcal{H}} M_l(c) \right), \quad (57)$$

where $M_l(c)$ is one if there is a dimer on the link l and zero otherwise, and \mathcal{V} and \mathcal{H} denote all vertical resp. horizontal links. On the other hand, in the high-temperature limit ($T \rightarrow \infty$) the partition function reduces to an unweighted sum over all allowed dimer configurations, the model is exactly solvable [56–58] and exhibits critical correlations [59] without any spatial symmetry breaking. A phase transition occurs between these two phases around temperature $T_c = 0.65$ [55, 60].

We can represent the partition function of the interacting dimer model by a tensor network with a bipartite sub-lattice structure. Indeed, if we choose the tensors A and B as

$$k \text{---} \textcircled{A} \text{---} i = \begin{cases} 1, & i = j + 1 = k + 2 = l + 3 \\ 0, & \text{else} \end{cases} \quad (58)$$

respectively

$$k \text{---} \textcircled{B} \text{---} i = \begin{cases} 1, & i = j - 1 = k - 2 = l - 3 \\ 0, & \text{else} \end{cases} \quad (59)$$

and define the matrix t as

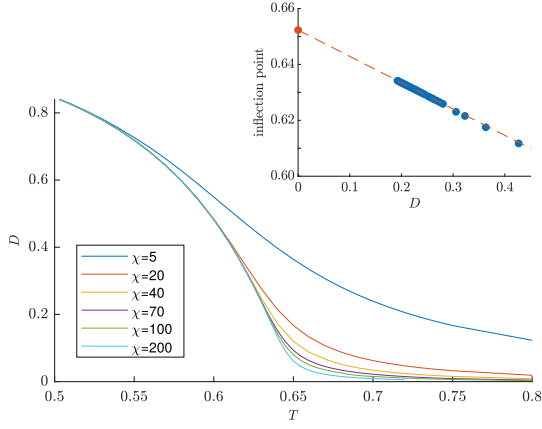


Figure 6: The order parameter D characterizing the columnar phase in the interacting dimer model as a function of temperature for different values of the bond dimension. In the inset we perform an extrapolation of the inflection point as a function of the bond dimension D , yielding an estimate for the critical point $T_c \approx 0.6523$.

$$\text{---} \textcircled{t} \text{---} = \begin{pmatrix} 1 & 0 & 0 & 0 \\ 0 & e^{\beta/2} & 1 & 1 \\ 0 & 1 & 1 & 1 \\ 0 & 1 & 1 & e^{\beta/2} \end{pmatrix} \quad (60)$$

we can define

$$\text{---} \textcircled{\tilde{A}} \text{---} = \text{---} \textcircled{q} \text{---} \textcircled{A} \text{---} \textcircled{q} \text{---} \quad (61)$$

with $q^2 = t$, and the analogical definition for \tilde{B} . Then the partition function Eq. (56) is given by

$$\mathcal{Z} = \begin{array}{c} \vdots \\ \dots \textcircled{\tilde{A}} \textcircled{\tilde{B}} \textcircled{\tilde{A}} \dots \\ \dots \textcircled{\tilde{B}} \textcircled{\tilde{A}} \textcircled{\tilde{B}} \dots \\ \dots \textcircled{\tilde{A}} \textcircled{\tilde{B}} \textcircled{\tilde{A}} \dots \\ \vdots \end{array} \quad (62)$$

This construction is seen to give the correct partition function by realizing that (i) a ‘1’ on a link denotes the presence of a dimer in that configuration, (ii) the tensors A and B guarantee that exactly one dimer is on each site, (iii) the $e^{\beta/2}$ factors in the t matrix introduce the correct Boltzmann weight when there are two parallel dimers on a plaquette.

Since we have a tensor network with a two-by-two unit cell and this model breaks translational symmetry at low temperatures, we apply the multisite VUMPS algorithm. In Fig. 7 we plot the probabilities of finding a dimer on the different links in the

lattice, showing columnar order for low temperatures and a uniform distribution in the high-temperature phase. In Fig. 6 we show the behaviour of the order parameter D for different values of the bond dimension, showing an increasingly critical form as the bond dimension increases. To determine the critical point we compare the temperature of the inflection point against the order parameter of the inflection point for different values of the bond dimension. We see that the temperature of the inflection point relates linearly with the value of the order parameter at that temperature. In the inset of Fig. 6 we provide an extrapolation of the critical point $T_c = 0.6523 \pm 0.0001$, which agrees with and improves upon known values in the literature.

4.3 Doped RVB state

For our third benchmark we start from the resonating valence bond (RVB) state in the square lattice, which can be represented as a translation-invariant PEPS from a local tensor $A_{u,r,d,l}^s$ with explicit $SU(2)$ invariance [61]. Following the framework of symmetric tensor networks, we can label the non-zero blocks in the tensor with $SU(2)$ irreducible representations; for the nearest-neighbour RVB we have only four non-zero blocks,

$$\begin{aligned} A_{\frac{1}{2},0,0,0}^{\frac{1}{2}} &= 1, & A_{0,\frac{1}{2},0,0}^{\frac{1}{2}} &= 1, \\ A_{0,0,\frac{1}{2},0}^{\frac{1}{2}} &= 1, & A_{0,0,0,\frac{1}{2}}^{\frac{1}{2}} &= 1. \end{aligned} \quad (63)$$

This state is known [61] to be in a critical $(2+0)$ -dimensional Coulomb phase and has power-law decaying dimer-dimer correlations. As a result, the contraction typically requires a large bond dimension for accurate results.

We now modify the RVB state by introducing holes on one of the two sub-lattices. This ‘doping’ is performed by introducing a second PEPS tensor B with non-zero blocks

$$B_{0,0,0,0}^0 = \lambda_1, \quad (64)$$

$$B_{\frac{1}{2},\frac{1}{2},0,0}^0 = \lambda_2, \quad B_{0,\frac{1}{2},\frac{1}{2},0}^0 = \lambda_2,$$

$$B_{0,0,\frac{1}{2},\frac{1}{2}}^0 = \lambda_2, \quad B_{\frac{1}{2},0,0,\frac{1}{2}}^0 = \lambda_2, \quad (65)$$

$$B_{0,\frac{1}{2},0,\frac{1}{2}}^0 = \lambda_3, \quad B_{\frac{1}{2},0,\frac{1}{2},0}^0 = \lambda_3. \quad (66)$$

The PEPS is then built up from the PEPS tensors $A_1 = A$ and $A_2 = A + B$ as

$$|\Psi(A_1, A_2)\rangle = \begin{array}{c} \vdots \\ \dots \textcircled{A_1} \textcircled{A_2} \textcircled{A_1} \dots \\ \dots \textcircled{A_2} \textcircled{A_1} \textcircled{A_2} \dots \\ \dots \textcircled{A_1} \textcircled{A_2} \textcircled{A_1} \dots \\ \vdots \end{array}, \quad (67)$$

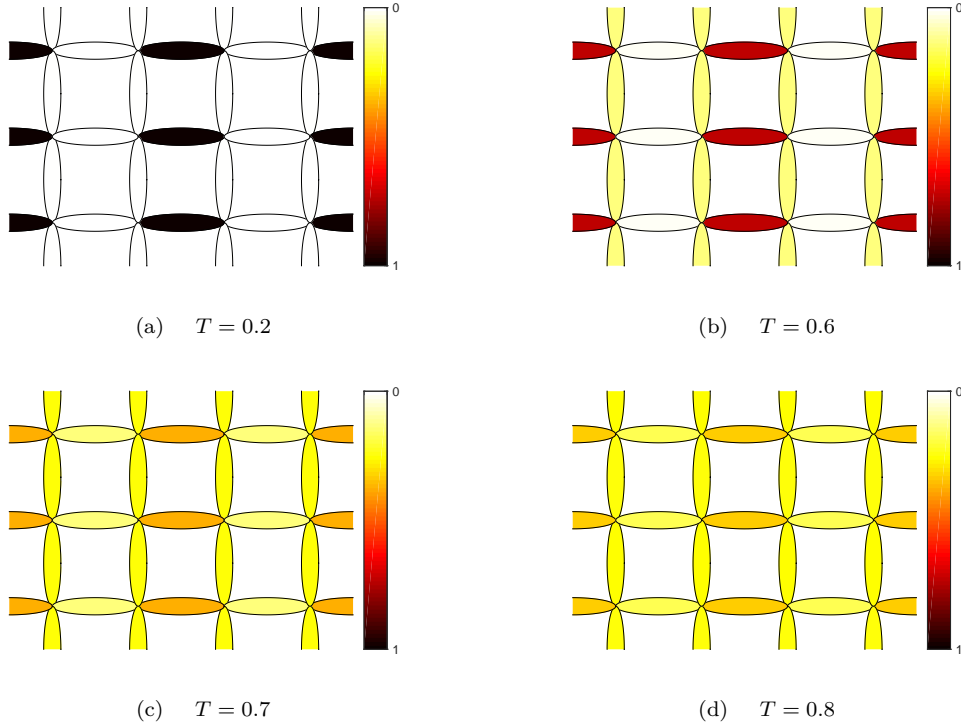


Figure 7: Probability (color scale) of finding a dimer on different links in the lattice for different temperatures, as computed by the VUMPS algorithm with bond dimension $\chi = 70$.

where the above blocks in the tensor B are chosen such that the state is rotation invariant. This state is similar to previous doping constructions, where a doping of the RVB state by unpaired spins [62] and fermionic holes [63] has been implemented in a translation-invariant way. Also, in contrast to the latter, we do not invoke any fermionic degrees of freedom in our state, so we effectively dope the state with bosonic holes on every second site.

Since this PEPS is non-translation-invariant by construction, we use the multi-site VUMPS algorithm for contracting it and computing observables. As an illustration, we fix the above three parameters to be the same ($\lambda_1 = \lambda_2 = \lambda_3 = \lambda$) and we compute the hole density (per site) as a function of the parameter λ . Because the undoped RVB state is critical, a large bond dimension for the boundaries is needed and we work with explicit $SU(2)$ invariant tensors in each step of the VUMPS algorithm. In Fig. 8 we plot the result, showing a slow onset that follows a power-law, as is illustrated by the inset log-log plot followed by a slow saturation to 1 as λ grows bigger, as is to be expected.

5 Conclusion and outlook

In this work, we have presented a generalization of the VUMPS algorithm for contracting two-dimensional tensor networks to the case of non-trivial unit cells.

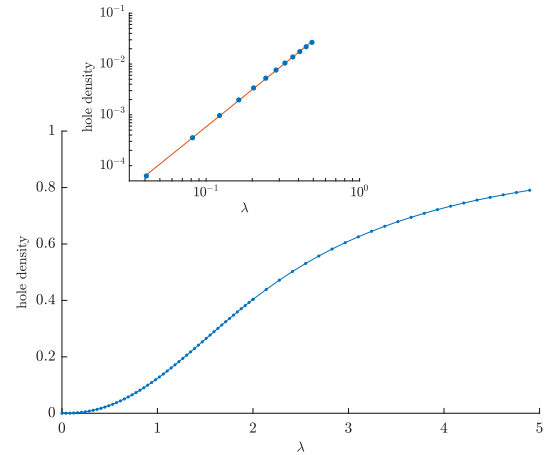


Figure 8: The hole density of the doped RVB state as a function of a single parameter λ . We have used a $SU(2)$ symmetric version of the multisite VUMPS algorithm with total bond dimensions ranging from 92 to 1414. For small λ we see a power law behaviour, as illustrated by the inset log-log plot (we find the exponent 2.43 ± 0.02).

The algorithm inherits the salient features of variational uniform MPS methods including optimality guarantees and high rates of convergence, while the computational effort scales only linearly with the size of the unit cell. We have benchmarked the contraction method on the square lattice antiferromagnetic Ising model, the phase transition in the square-lattice interacting dimer model and on the doped RVB PEPS. We expect this algorithm to be important in the simulation of quantum spin systems in two-dimensions with PEPS, wherever larger unit cells are required for the representation of the ground state, as well as for the simulation of classical two-dimensional systems where a unit cell appears either in the representation of the partition function or due to symmetry breaking. We hope that the emulation technique of larger unit cells presented in this work inspires further generalizations of known tensor network methods to larger unit cells.

Acknowledgments

AN thanks A. Bauer for stimulating discussions and proofreading and is grateful to the ObstOffice for a fruitful and juicy environment. This work is supported by the Research Foundation Flanders, ERC grants QUTE (No. 647905), the DFG (CRC 183, EI 519/15-1), the Templeton Foundation, and EU Grant SIQS.

References

- [1] S. R. White. Density matrix formulation for quantum renormalization groups. *Phys. Rev. Lett.*, 69:2863–2866, Nov 1992. DOI: [10.1103/PhysRevLett.69.2863](https://doi.org/10.1103/PhysRevLett.69.2863).
- [2] F. Verstraete, J. I. Cirac, and V. Murg. Matrix product states, projected entangled pair states, and variational renormalization group methods for quantum spin systems. *Adv. Phys.*, 57:143, 2008. DOI: [10.1080/14789940801912366](https://doi.org/10.1080/14789940801912366).
- [3] R. Orús. A practical introduction to tensor networks: Matrix product states and projected entangled pair states. *Ann. Phys.*, 349:117–158, 2014. DOI: [10.1016/j.aop.2014.06.013](https://doi.org/10.1016/j.aop.2014.06.013).
- [4] N. Schuch. *Lecture notes for the 44th IFF Spring School “Quantum Information Processing” in Juelich*, 2013.
- [5] J. Eisert. Entanglement and tensor network states. *Modeling and Simulation*, 3:520, 2013.
- [6] J. C. Bridgeman and C. T. Chubb. Hand-waving and interpretive dance: An introductory course on tensor networks. *J. Phys. A*, 50:223001, 2017. DOI: [10.1088/1751-8121/aa6dc3](https://doi.org/10.1088/1751-8121/aa6dc3).
- [7] U. Schollwöck. The density-matrix renormalization group in the age of matrix product states. *Ann. Phys.*, 326(1):96–192, 2011. ISSN 0003-4916. DOI: <https://doi.org/10.1016/j.aop.2010.09.012>.
- [8] F. Pollmann and A. M. Turner. Detection of symmetry-protected topological phases in one dimension. *Phys. Rev. B*, 86:125441, 2012. DOI: [10.1103/PhysRevB.86.125441](https://doi.org/10.1103/PhysRevB.86.125441).
- [9] N. Schuch, D. Pérez-García, and I. Cirac. Classifying quantum phases using matrix product states and projected entangled pair states. *Phys. Rev. B*, 84:165139, Oct 2011. DOI: [10.1103/PhysRevB.84.165139](https://doi.org/10.1103/PhysRevB.84.165139).
- [10] A. Nietner, C. Krumnow, E. J. Bergholtz, and J. Eisert. Composite symmetry-protected topological order and effective models. *Phys. Rev. B*, 96:235138, 2017. DOI: [10.1103/PhysRevB.96.235138](https://doi.org/10.1103/PhysRevB.96.235138).
- [11] P. Corboz and F. Mila. Crystals of bound states in the magnetization plateaus of the shastry-sutherland model. *Phys. Rev. Lett.*, 112:147203, Apr 2014. DOI: [10.1103/PhysRevLett.112.147203](https://doi.org/10.1103/PhysRevLett.112.147203).
- [12] P. Corboz, T. M. Rice, and M. Troyer. Competing states in the t - j model: Uniform d -wave state versus stripe state. *Phys. Rev. Lett.*, 113:046402, Jul 2014. DOI: [10.1103/PhysRevLett.113.046402](https://doi.org/10.1103/PhysRevLett.113.046402).
- [13] L. Vanderstraeten, J. Haegeman, P. Corboz, and F. Verstraete. Gradient methods for variational optimization of projected entangled-pair states. *Phys. Rev. B*, 94:155123, Oct 2016. DOI: [10.1103/PhysRevB.94.155123](https://doi.org/10.1103/PhysRevB.94.155123).
- [14] A. Kshetrimayum, C. Balz, B. Lake, and J. Eisert. Tensor network investigation of the double layer Kagome compound $\text{Ca}_{10}\text{Cr}_7\text{O}_{28}$. 2019.
- [15] P. Czarnik, J. Dziarmaga, and P. Corboz. Time evolution of an infinite projected entangled pair state: An efficient algorithm. *Phys. Rev. B*, 99:035115, Jan 2019. DOI: [10.1103/PhysRevB.99.035115](https://doi.org/10.1103/PhysRevB.99.035115).
- [16] C. Hubig and J. I. Cirac. Time-dependent study of disordered models with infinite projected entangled pair states. *SciPost Phys.*, 6:31, 2019. DOI: [10.21468/SciPostPhys.6.3.031](https://doi.org/10.21468/SciPostPhys.6.3.031).
- [17] A. Kshetrimayum, M. Goihl, and J. Eisert. Time evolution of many-body localized systems in two spatial dimensions. 2019.
- [18] L. Vanderstraeten, M. Mariën, F. Verstraete, and J. Haegeman. Excitations and the tangent space of projected entangled-pair states. *Phys. Rev. B*, 92:201111, Nov 2015. DOI: [10.1103/PhysRevB.92.201111](https://doi.org/10.1103/PhysRevB.92.201111).
- [19] L. Vanderstraeten, J. Haegeman, and F. Verstraete. Simulating excitation spectra with projected entangled-pair states. *Phys. Rev. B*, 99:165121, Apr 2019. DOI: [10.1103/PhysRevB.99.165121](https://doi.org/10.1103/PhysRevB.99.165121).
- [20] A. Kshetrimayum, M. Rizzi, J. Eisert, and R. Orús. Tensor network annealing algorithm

- for two-dimensional thermal states. *Phys. Rev. Lett.*, 122:070502, Feb 2019. DOI: [10.1103/PhysRevLett.122.070502](https://doi.org/10.1103/PhysRevLett.122.070502).
- [21] Piotr Czarnik, Lukasz Cincio, and Jacek Dziarmaga. Projected entangled pair states at finite temperature: Imaginary time evolution with ancillas. *Phys. Rev. B*, 86:245101, Dec 2012. DOI: [10.1103/PhysRevB.86.245101](https://doi.org/10.1103/PhysRevB.86.245101).
- [22] A. Kshetrimayum, H. Weimer, and R. Orus. A simple tensor network algorithm for 2d steady states. *Nature Comm.*, 8:1291, 2017. DOI: [10.1038/s41467-017-01511-6](https://doi.org/10.1038/s41467-017-01511-6).
- [23] T. Nishino. Density matrix renormalization group method for 2d classical models. *J. Phys. Soc. Jap.*, 64(10):3598–3601, 1995. DOI: [10.1143/JPSJ.64.3598](https://doi.org/10.1143/JPSJ.64.3598).
- [24] T. Nishino, Y. Hieida, K. Okunishi, N. Maeshima, Y. Akutsu, and A. Gendiar. Two-dimensional tensor product variational formulation. *Prog. Th. Phys.*, 105(3):409–417, 03 2001. DOI: [10.1143/PTP.105.409](https://doi.org/10.1143/PTP.105.409).
- [25] L. Vanderstraeten, B. Vanhecke, and F. Verstraete. Residual entropies for three-dimensional frustrated spin systems with tensor networks. *Phys. Rev. E*, 98:042145, Oct 2018. DOI: [10.1103/PhysRevE.98.042145](https://doi.org/10.1103/PhysRevE.98.042145).
- [26] M. Levin and Cody P. Nave. Tensor renormalization group approach to two-dimensional classical lattice models. *Phys. Rev. Lett.*, 99:120601, Sep 2007. DOI: [10.1103/PhysRevLett.99.120601](https://doi.org/10.1103/PhysRevLett.99.120601).
- [27] Z. Y. Xie, J. Chen, M. P. Qin, J. W. Zhu, L. P. Yang, and T. Xiang. Coarse-graining renormalization by higher-order singular value decomposition. *Phys. Rev. B*, 86:045139, Jul 2012. DOI: [10.1103/PhysRevB.86.045139](https://doi.org/10.1103/PhysRevB.86.045139).
- [28] G. Evenbly and G. Vidal. Tensor network renormalization. *Phys. Rev. Lett.*, 115:180405, Oct 2015. DOI: [10.1103/PhysRevLett.115.180405](https://doi.org/10.1103/PhysRevLett.115.180405).
- [29] S. Yang, Z.-G. Gu, and X.-G. Wen. Loop optimization for tensor network renormalization. *Phys. Rev. Lett.*, 118:110504, Mar 2017. DOI: [10.1103/PhysRevLett.118.110504](https://doi.org/10.1103/PhysRevLett.118.110504).
- [30] M. Bal, M. Mariën, J. Haegeman, and F. Verstraete. Renormalization group flows of hamiltonians using tensor networks. *Phys. Rev. Lett.*, 118:250602, Jun 2017. DOI: [10.1103/PhysRevLett.118.250602](https://doi.org/10.1103/PhysRevLett.118.250602).
- [31] M. Hauru, C. Delcamp, and S. Mizera. Renormalization of tensor networks using graph-independent local truncations. *Phys. Rev. B*, 97:045111, Jan 2018. DOI: [10.1103/PhysRevB.97.045111](https://doi.org/10.1103/PhysRevB.97.045111).
- [32] R. J. Baxter. Dimers on a rectangular lattice. *J. Math. Phys.*, 9(4):650–654, 1968. DOI: [10.1063/1.1664623](https://doi.org/10.1063/1.1664623).
- [33] R. J. Baxter. Variational approximations for square lattice models in statistical mechanics. *J. Stat. Phys.*, 19:461–478, Nov 1978. ISSN 1572-9613. DOI: [10.1007/BF01011693](https://doi.org/10.1007/BF01011693).
- [34] T. Nishino and K. Okunishi. Corner transfer matrix renormalization group method. *J. Phys. Soc. Jap.*, 65(4):891–894, 1996. DOI: [10.1143/JPSJ.65.891](https://doi.org/10.1143/JPSJ.65.891).
- [35] T. Nishino and K. Okunishi. Corner transfer matrix algorithm for classical renormalization group. *J. Phys. Soc. Jap.*, 66(10):3040–3047, 1997. DOI: [10.1143/JPSJ.66.3040](https://doi.org/10.1143/JPSJ.66.3040).
- [36] R. Orús and G. Vidal. Simulation of two-dimensional quantum systems on an infinite lattice revisited: Corner transfer matrix for tensor contraction. *Phys. Rev. B*, 80:094403, Sep 2009. DOI: [10.1103/PhysRevB.80.094403](https://doi.org/10.1103/PhysRevB.80.094403).
- [37] P. Corboz, J. Jordan, and G. Vidal. Simulation of fermionic lattice models in two dimensions with projected entangled-pair states: Next-nearest neighbor hamiltonians. *Phys. Rev. B*, 82:245119, Dec 2010. DOI: [10.1103/PhysRevB.82.245119](https://doi.org/10.1103/PhysRevB.82.245119).
- [38] Guifré Vidal. Efficient classical simulation of slightly entangled quantum computations. *Phys. Rev. Lett.*, 91:147902, Oct 2003. DOI: [10.1103/PhysRevLett.91.147902](https://doi.org/10.1103/PhysRevLett.91.147902).
- [39] R. Orús and G. Vidal. Infinite time-evolving block decimation algorithm beyond unitary evolution. *Phys. Rev. B*, 78:155117, Oct 2008. DOI: [10.1103/PhysRevB.78.155117](https://doi.org/10.1103/PhysRevB.78.155117).
- [40] Shi-Ju Ran. Ab initio optimization principle for the ground states of translationally invariant strongly correlated quantum lattice models. *Phys. Rev. E*, 93:053310, May 2016. DOI: [10.1103/PhysRevE.93.053310](https://doi.org/10.1103/PhysRevE.93.053310).
- [41] Shi-Ju Ran, Emanuele Tirrito, Cheng Peng, Xi Chen, Gang Su, and Maciej Lewenstein. Tensor network contractions. *Lecture Notes in Physics*, 2020. DOI: [10.1007/978-3-030-34489-4](https://doi.org/10.1007/978-3-030-34489-4).
- [42] V. Zauner-Stauber, L. Vanderstraeten, M. T. Fishman, F. Verstraete, and J. Haegeman. Variational optimization algorithms for uniform matrix product states. *Phys. Rev. B*, 97:045145, Jan 2018. DOI: [10.1103/PhysRevB.97.045145](https://doi.org/10.1103/PhysRevB.97.045145).
- [43] J. Haegeman, C. Lubich, I. Oseledets, B. Vandereycken, and F. Verstraete. Unifying time evolution and optimization with matrix product states. *Phys. Rev. B*, 94:165116, Oct 2016. DOI: [10.1103/PhysRevB.94.165116](https://doi.org/10.1103/PhysRevB.94.165116).
- [44] L. Vanderstraeten, J. Haegeman, and F. Verstraete. Tangent-space methods for uniform matrix product states. *SciPost Phys. Lect. Notes*, page 7, 2019. DOI: [10.21468/SciPostPhysLectNotes.7](https://doi.org/10.21468/SciPostPhysLectNotes.7).
- [45] M. T. Fishman, L. Vanderstraeten, V. Zauner-Stauber, J. Haegeman, and F. Verstraete. Faster methods for contracting infinite two-dimensional tensor networks. *Phys. Rev. B*, 98:235148, Dec 2018. DOI: [10.1103/PhysRevB.98.235148](https://doi.org/10.1103/PhysRevB.98.235148).

- [46] P. Corboz, S. R. White, G. Vidal, and M. Troyer. Stripes in the two-dimensional t - j model with infinite projected entangled-pair states. *Phys. Rev. B*, 84:041108, Jul 2011. DOI: [10.1103/PhysRevB.84.041108](https://doi.org/10.1103/PhysRevB.84.041108).
- [47] A. Bauer, J. Eisert, and C. Wille. Towards a mathematical formalism for classifying phases of matter. 2019.
- [48] M. B. Hastings and T. Koma. Spectral gap and exponential decay of correlations. *Comm. Math. Phys.*, 265(3):781–804, 2006. DOI: [10.1007/s00220-006-0030-4](https://doi.org/10.1007/s00220-006-0030-4).
- [49] F. G. S. L. Brandão and M. Horodecki. Exponential decay of correlations implies area law. *Comm. Math. Phys.*, 333:761–798, Jan 2015. ISSN 1432-0916. DOI: [10.1007/s00220-014-2213-8](https://doi.org/10.1007/s00220-014-2213-8).
- [50] N. Schuch and F. Verstraete. Matrix product state approximations for infinite systems. 2017.
- [51] Alexander M Dalzell and Fernando GSL Brandão. Locally accurate mps approximations for ground states of one-dimensional gapped local hamiltonians. *Quantum*, 3:187, 2019. DOI: <https://doi.org/10.22331/q-2019-09-23-187>.
- [52] Y. Huang. Approximating local properties by tensor network states with constant bond dimension. 2019.
- [53] J. Haegeman, T. J. Osborne, and F. Verstraete. Post-matrix product state methods: To tangent space and beyond. *Phys. Rev. B*, 88:075133, Aug 2013. DOI: [10.1103/PhysRevB.88.075133](https://doi.org/10.1103/PhysRevB.88.075133).
- [54] F. Alet, J. Lykke Jacobsen, G. Misguich, V. Pasquier, F. Mila, and M. Troyer. Interacting classical dimers on the square lattice. *Phys. Rev. Lett.*, 94:235702, Jun 2005. DOI: [10.1103/PhysRevLett.94.235702](https://doi.org/10.1103/PhysRevLett.94.235702).
- [55] F. Alet, Y. Ikhlef, J. L. Jacobsen, G. Misguich, and V. Pasquier. Classical dimers with aligning interactions on the square lattice. *Phys. Rev. E*, 74:041124, Oct 2006. DOI: [10.1103/PhysRevE.74.041124](https://doi.org/10.1103/PhysRevE.74.041124).
- [56] P. W. Kasteleyn. The statistics of dimers on a lattice: I. the number of dimer arrangements on a quadratic lattice. *Physica*, 27(12):1209 – 1225, 1961. ISSN 0031-8914. DOI: [https://doi.org/10.1016/0031-8914\(61\)90063-5](https://doi.org/10.1016/0031-8914(61)90063-5).
- [57] H. N. V. Temperley and M. E. Fisher. Dimer problem in statistical mechanics-an exact result. *Phil. Mag. A*, 6(68):1061–1063, 1961. DOI: [10.1080/14786436108243366](https://doi.org/10.1080/14786436108243366).
- [58] M. E. Fisher. Statistical mechanics of dimers on a plane lattice. *Phys. Rev.*, 124:1664–1672, Dec 1961. DOI: [10.1103/PhysRev.124.1664](https://doi.org/10.1103/PhysRev.124.1664).
- [59] M. E. Fisher and John Stephenson. Statistical mechanics of dimers on a plane lattice. ii. dimer correlations and monomers. *Phys. Rev.*, 132:1411–1431, 1963. DOI: [10.1103/PhysRev.132.1411](https://doi.org/10.1103/PhysRev.132.1411).
- [60] Y. Li, D. Wu, X. Huang, and C. Ding. Percolation of interacting classical dimers on the square lattice. *Physica A*, 404:285 – 290, 2014. ISSN 0378-4371. DOI: <https://doi.org/10.1016/j.physa.2014.02.076>.
- [61] N. Schuch, D. Poilblanc, J. I. Cirac, and D. Pérez-García. Resonating valence bond states in the PEPS formalism. *Phys. Rev. B*, 86:115108, Sep 2012. DOI: [10.1103/PhysRevB.86.115108](https://doi.org/10.1103/PhysRevB.86.115108).
- [62] D. Poilblanc. Entanglement Hamiltonian of the quantum Néel state. *J. Stat. Mech.*, 2014 (10):P10026, oct 2014. DOI: [10.1088/1742-5468/2014/10/p10026](https://doi.org/10.1088/1742-5468/2014/10/p10026).
- [63] D. Poilblanc, P. Corboz, N. Schuch, and J. I. Cirac. Resonating-valence-bond superconductors with fermionic projected entangled pair states. *Phys. Rev. B*, 89:241106, Jun 2014. DOI: [10.1103/PhysRevB.89.241106](https://doi.org/10.1103/PhysRevB.89.241106).

A Derivation of the generalized fixed point equations

In this appendix, we are going to give an alternative to the derivation of the optimality criterion of the VUMPS algorithm and thereby generalize it to non-trivial unit cells. In Section A.1 we will generalize the reasoning from Ref. [42] to non-hermitian transfer operators. In Section A.2 we will further generalize to non-trivial unit cells. An alternative derivation of the fixed point equations for a non-trivial unit cell using the emulation of non-trivial unit cell tensor networks with trivial unit cell tensor networks which is based on the single site VUMPS algorithm with non-hermitian transfer operators is given in Appendix B.

A.1 VUMPS for non-hermitian transfer matrices

The VUMPS algorithm [42] is a scheme to optimize the equation

$$\mathcal{P}_A(M - \lambda) |\psi(A)\rangle = 0 \quad (68)$$

via iterating over local tensor equations. Here A is the tensor parametrizing the state vector $|\psi(A)\rangle$, M is the MPO for which we wish to find an approximation of the boundary, λ is the corresponding maximal eigenvalue and \mathcal{P}_A is the projector onto the tangent space of the MPS manifold at the point parametrized by A as in Eq. (23). Eq. (68) can be shown to be the variational optimum approximating the boundary of the tensor network parametrized by M over the MPS manifold for any given fixed bond dimension given that the MPO transfer matrix defined through M is hermitian [42]. In the following, we are going to show that this holds true also if the MPO transfer matrix defined through M ceases to be hermitian but is gapped, in the sense that the absolute values of the eigenvalues of the MPO transfer matrix still sustain a gap stable in the asymptotic limit. This situation can reflect a classical partition function of a non-critical Ising model or the double layer sandwich of the toric code PEPS.

For the contraction of the tensor network, we are interested in its boundary which is the maximal eigenvector of the MPO transfer matrix. More precisely, the boundary $|\phi\rangle$ is the eigenvector corresponding to the largest eigenvalue of M in absolute value

$$M |\phi\rangle \propto |\phi\rangle \quad (69)$$

This, in turn, corresponds to the resulting state upon an infinite application of the MPO transfer matrix on a suitably chosen random initial state. Moreover, for topological fixed point models, the maximal eigenvectors correspond to the topological boundaries of the model. Those are the states that live on the boundary if one computed observables of this model on a manifold with a boundary.

Because the MPO is gapped in the above sense, the boundary will feature exponentially decaying correlations. The exponentially decaying correlations of the one dimensional boundary, however, imply that we can faithfully approximate it locally by an MPS. More precisely, the reduced density matrix of the many body state with exponential correlations on segments of length k is ϵ -close to an MPS with bond dimension scaling as $\mathcal{O}(k/\epsilon^3)$ [49–52]. So in this sense, being interested only in k -local properties we can write the state explicitly as an MPS with an error smaller than ϵ .

Hence, for large enough k and at a sufficiently large bond dimension χ such that the corresponding (k, ϵ) approximation error is below machine precision, we are practically not able to computationally distinguish the MPS $|\psi(A)\rangle$ from the true boundary state vector $|\phi\rangle$. Hence, we argue that we can apply the fixed point equation Eq. (69) to $|\psi(A)\rangle$

$$M |\psi(A)\rangle \approx \lambda |\psi(A)\rangle \quad (70)$$

where the approximation error due to the application of M might increase from ϵ to some $\epsilon' > \epsilon$, though the increase will be in a controlled way given that M is gapped. This can be understood as follows. The state vector $|\psi(A)\rangle$ is (k, ϵ) -close to $|\phi\rangle$. Additionally, the application of M exponentially suppresses the overlap orthogonal to its maximal eigenstate. Hence, the normalized $M |\psi(A)\rangle$ is closer to $|\phi\rangle$ than $|\psi(A)\rangle$ is. Therefore, the normalized $M |\psi(A)\rangle$ will be $(k', \epsilon'/2)$ close to $|\phi\rangle$, up to boundary effects (at the boundary of the local patch of size k) decaying exponentially in the depth into the region, leading to a modified $\epsilon'/2$, and hence at most (k', ϵ') -far from $|\psi(A)\rangle$. Hence, if k and χ are chosen sufficiently large, the resulting $\epsilon' > 0$ will still be below machine precision, while k' will still be sufficiently large.

As we are working over the manifold of MPS, it is natural to use the tangent space projector in order to reduce the fixed point Eq. (70) from a many body Hilbert space equation to a finite equation. The resulting equation still resolves the overlap of $M |\psi(A)\rangle$ with the full manifold of MPS whilst only neglecting states that cannot be captured by the manifold of MPS. Hence, we obtain Eq. (68). Similarly as before, one might argue that the projector is not a local operator and hence one might not be able to apply the (k, ϵ) -closeness. However, we can construct a similar argument as for the MPO transfer matrix applied to the MPS in Eq. (70). For each term in the sum of the projector (cf. Eq. (23)) applied to the MPS, we find that essentially only a finite patch contributes to the projector because the gap in the MPS-MPO-MPS transfer matrix exponentially suppresses the contribution of the tail of the transfer matrix channel.

It is interesting to note that the above reasoning could be generalized even further to critical systems, at the price of a polynomial rather than a linear de-

pendence on the bond dimension [52]. Also, for critical systems, the application of M does not exponentially suppress the overlap orthogonal to the boundary but only in a weaker sense. To conclude, we find that the optimality criterion the VUMPS algorithm optimizes can also be understood for non-hermitian gapped MPOs.

A.2 Non-trivial unit cells: A variational argument

As explained in Section 3.2, in order to find the boundary of a tensor network with a non-trivial unit cell we need to find a $|\psi_1\rangle$ and λ that satisfy $M_n \dots M_2 M_1 |\psi_1\rangle = \lambda |\psi_1\rangle$, where the M_i are MPOs or MPO-like objects defining the tensor network. We do this by assuming $|\psi_1\rangle$ is well captured by an MPS $|\psi(A_1)\rangle$, which may be motivated through arguments similar as in Appendix A.1. As explained before, this is equivalent to looking for a set of MPSs $|\psi(A_i)\rangle$ and scalars γ_i satisfying

$$\begin{aligned} M_1 |\psi(A_1)\rangle &\approx \gamma_1 |\psi(A_2)\rangle, \\ M_2 |\psi(A_2)\rangle &\approx \gamma_2 |\psi(A_3)\rangle, \\ &\dots \\ M_n |\psi(A_n)\rangle &\approx \gamma_n |\psi(A_1)\rangle, \end{aligned} \quad (71)$$

with $\prod_i \gamma_i = \lambda$. We use the approximate sign in order to emphasize that $|\psi(A_{i+1})\rangle$ approximates $M_i |\psi(A_i)\rangle$ in some sort of optimal way. In this text we choose the meaning of this optimality to be variational in the sense of the fidelity per site in the thermodynamic limit. In particular,

$$\lim_{N \rightarrow \infty} |\langle \psi^N(A_{i+1}) | M_i | \psi^N(A_i) \rangle|^{1/N} \quad (72)$$

should be maximal with respect to A_{i+1} .

Having thus translated the problem to variational MPS [44] we can formulate a first naive algorithm to find the boundary. Start with some initial MPS $|\psi(A_1^{(0)})\rangle$ and consecutively apply all the M_i each time followed by variationally approximating the new MPS by maximizing the fidelity per site by another MPS of some given bond dimension. Repeat that procedure until convergence is reached. Clearly, this power method will eventually converge to the fixed point characterized by the Eq. (71).

Similarly to the derivation of the VUMPS algorithm [42] we find the optimality criterion of maximizing the fidelity per site to be equivalent to the vanishing of the tangent space projector on the fixed point equation. In particular, for the variationally optimal solution A_i to Eq. (71) it must hold

$$\mathcal{P}_{A_{i+1}}(M_i |\psi(A_i)\rangle - \gamma_i |\psi(A_{i+1})\rangle) = 0 \quad (73)$$

where \mathcal{P}_A represents the MPS-tangent space projector at the state parametrized by A . In this particular case the tangent space criterion is equivalent to maximizing the fidelity per site. Note, however, that the tangent space criterion need not imply a variational principle in general.

Instead of the just described power method however we go one step further: we write down all the fixed point equations Eq. (71) in the projected form of Eq. (73) at once, and call this our new, global fixed point equation. This can then be solved iteratively in a similar spirit as the original VUMPS algorithm as explained in Section 3.3. It is easy to see that the set of these global fixed point equations corresponds to 44 and 45. Obviously, as Eq. (73) is contained in the global fixed point equation a solution to this global fixed point equation contains the result of the above described power method.

B Tensor networks with non-trivial unit cell

In this appendix we will formally generalize the VUMPS method to tensor networks that admit a non-trivial unit cell. Instead of arguing from a power method as in Appendix A.2 we will be using the emulation of non-trivial unit cell tensor networks by trivial unit cell tensor networks. It will be easy to see that the cost scales only linearly rather than an exponential in the unit cell size. In this work, we assume that the lattice on which the tensor network is defined still has the same regularity within the unit cell as on the outer level connecting those unit cells, both having rectangular structure.

B.1 Emulating tensor networks with a non-trivial unit cell by tensor networks with a trivial unit cell

In order to apply the VUMPS methodology to tensor networks with a non-trivial unit cell we are going to emulate the latter by a tensor network with a trivial unit cell. However, instead of achieving this by merely blocking the tensors within one unit cell – leading to an exponential overhead in the complexity – we are going to define a new model with a tensor network with a richer structure leading only to a linear overhead.

To start with, we observe that the data of a two dimensional tensor network on a rectangular lattice is defined by a four leg tensor for any position in the unit cell. In particular, this data can be modeled by a five leg tensor,

of non-trivial unit cell MPS with bond dimension χ and unit cell shape (n_x, n_y) which we denote by $\mathcal{M}_{n_x, n_y, \chi}$. Using this tensor network the fixed point equation then reads

$$\dots \oplus \dots \oplus \dots \oplus \dots \approx \gamma \dots \oplus \dots \oplus \dots \oplus \dots \quad (79)$$

Using $+^T = -$ and the fact that the y legs are all connected through delta tensors only we find that Eq. (79) is equivalent to Eq. (42). Note that if the MPO in Eq. (79) is not *normalized* such that it maps the y -th normalized boundary MPS to the normalized $y + 1$ 'st boundary MPS we must allow the boundary MPS to be not normalized within the unit cell channels in order to absorb the different scalar factors from the MPOs in each y channel similar to Eq. (40).

B.2 Geometry of MPS with non trivial unit cell tensors

As explained in the previous section we are going to work not on the usual manifold of MPS but on the manifold of MPS with non-trivial unit cell tensors $\mathcal{M}_{n_x, n_y, \chi}$. Therefore, let us re-derive the geometric picture of MPS on the new manifold $\mathcal{M}_{n_x, n_y, \chi}$ similar as in Ref. [44]. To this end, we are mainly interested in the tangent space projector on $\mathcal{M}_{n_x, n_y, \chi}$. It is straightforward to compute the tangent vectors $|\phi(B, A)\rangle$ at the point $|\psi(A)\rangle$. They are given by the equal weight superposition of all displacements of defects on $|\psi(A)\rangle$ with a given defect tensor B

$$|\phi(B, A)\rangle = \sum_{x, y, \alpha, s, \beta} B_{x, y, \alpha, s, \beta} \frac{\partial}{\partial A_{x, y, \alpha, s, \beta}} |\psi(A)\rangle = \sum_{n \in \mathbb{Z}} \dots \oplus \dots \oplus \dots \oplus \dots \quad (80)$$

where n indicates the site on which the defect matrix is placed. Due to the normalization of the MPS manifold the tangent space $\mathcal{T}_A \mathcal{M}_{n_x, n_y, \chi}$ at a point $|\psi(A)\rangle$ must be orthogonal in Hilbert space to the state parametrized by that point. This, together with the gauge degree of freedom in the MPS eliminates $\chi^2 n_x n_y$ degrees of freedom from the original $\chi^2 d n_x n_y$ degrees of freedom. This can be addressed directly by requiring that for the tensor B in Eq. (80) it must hold

$$\dots \oplus \dots \oplus \dots \oplus \dots = 0 \quad (81)$$

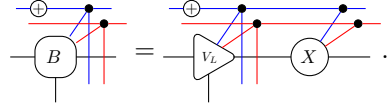
and vice versa for the same diagram flipped about the horizontal axis. In particular, B must have support on the null space of A_L only. In order to parametrize such tensors B we can define the tensor V_L similar to Ref. [44] to be an isometry on the null space of A_L at each (x, y) . Hence, for V_L it must hold

$$\dots \oplus \dots \oplus \dots \oplus \dots = 0 \quad (82)$$

and

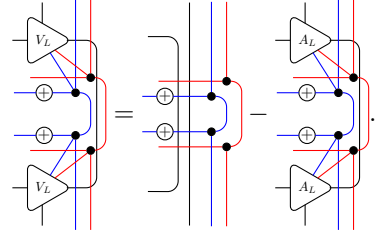
$$\dots \oplus \dots \oplus \dots \oplus \dots = \dots \quad (83)$$

As the null space of each of the $n_x n_y$ A_L is $\chi(d-1)$ dimensional, the right bond of V_L at (n_x, n_y) has dimension $\chi(d-1)$. Finally, we can write the parametrization of B using the $n_x n_y$ matrices X_{n_x, n_y} with dimensions $\chi(d-1) \times \chi$ fixing the free degrees of freedom of B as



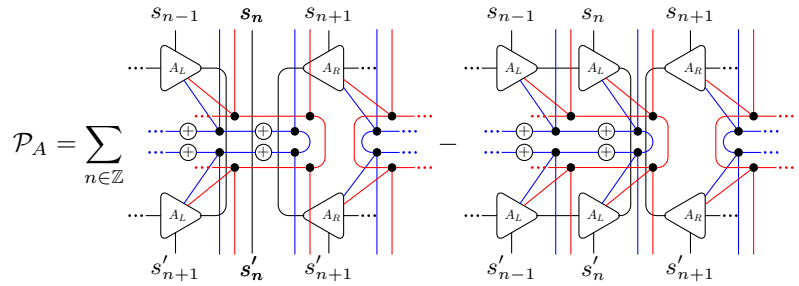
$$B = V_L \cdot X \quad (84)$$

Similarly as in Ref. [44], we can rewrite the projector onto the null space as



$$\quad (85)$$

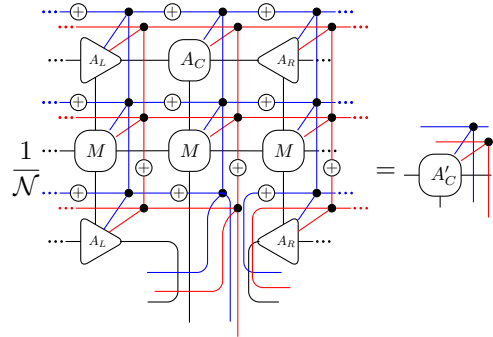
This is, we can straightforwardly use V_L in order to write the tangent space projector \mathcal{P}_A at point $|\psi(A)\rangle$ acting on states of the form as in Eq. (78) explicitly as



$$\mathcal{P}_A = \sum_{n \in \mathbb{Z}} \quad (86)$$

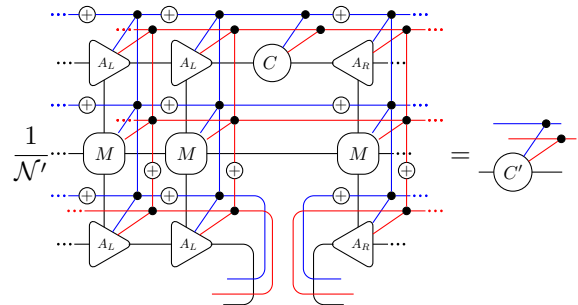
B.3 Multisite VUMPS in explicit notation

In order to derive the local VUMPS equations for the generalized tensor network we can combine the above Sections A.1, B.1 and B.2. Similar as for standard VUMPS we define the tensors A'_C and C' as



$$\frac{1}{\mathcal{N}} \quad (87)$$

and



$$\frac{1}{\mathcal{N}'} \quad (88)$$

where the diverging \mathcal{N} and \mathcal{N}' denote the normalizations counteracting the non-normalized transfer matrices as before. It is worth noticing that due to the substructure in the tensor network spanned by the x - and

Algorithm 3: Explicit terms of the local Hamiltonians in the sequential implementation.

Function `local_apply_h_a_c`((A_C^y) $_y$, x):
┌ (A_C^y) $_y$ \leftarrow update according to (48) at x
└ **return** (A_C^y) $_y$

Function `local_apply_h_c`((C^y) $_y$, x):
┌ (C^y) $_y$ \leftarrow update according to (49) at x
└ **return** (C^y) $_y$

parallel update has a smaller overhead per iteration computationally, because the environment terms need to be computed only once, the sequential algorithm seems to find short cuts in the iteration trajectory resulting in less iterations necessary till convergence. This can be understood nicely using the picture of Appendix B: While the parallel update corresponds to the minimization with respect to the full tangent space projector Eq. (86), the sequential update breaks these updates into optimizations with respect to hyperplanes within the tangent space (as the x -channel in the projector is fixed) with the consecutive updates in the x -direction being coupled. This means that for the sequential update there is more freedom to find different iteration trajectories, which however in general are not guaranteed to be shorter. It is easy to see that a solution of one algorithm is also a solution to the other algorithm.

While the understanding carries over, the findings cannot be applied straightforwardly to this work. Here we are dealing with MPOs rather than local Hamiltonians. In turn, the environment equations are as complex as the leading terms in complexity, the computation of A_C . Therefore, the environment terms are a leading term in complexity such that the sequential implementation scales quadratically in n_x . Note: The sequential algorithm in Ref. [42] scales quadratically in n_x , too, but only in a sub-leading term. For n_x sufficiently larger than the physical dimension, however, the parallel update can be expected to perform better than the sequential update in their case. Obviously in our case it still holds that both algorithms converge to the same solutions.

Algorithm 4: Sequential implementation of the VUMPS algorithm for non-trivial unit cells.

Data: MPO $M = (M_{x,y})_{x,y}$ with non-trivial (n_x, n_y) shaped unit cell; desired accuracy ϵ_{prec}

Result: Array containing the data of n_y MPS corresponding to the boundaries $(|\psi(A_y)\rangle\rangle_y$

$(|\psi(A_y)\rangle\rangle_y \leftarrow$ initialize MPS array

$(L_{x,y})_{x,y}, (R_{x,y})_{x,y} \leftarrow$ update environments from $\{(|\psi(A_y)\rangle\rangle_y, M\}$ calling `environment_terms`

$\epsilon_{gauge} \leftarrow 1$

$(\epsilon_{gauge,y})_y \leftarrow (1)_y$

while $\epsilon_{gauge} > \epsilon_{prec}$ **do**

for $x \in \{0, \dots, n_x\}$ **do**

$(A_C^{x,y})_y \leftarrow$ solve h_{A_C} using an iterative solver calling `local_apply_h_a_c` at x

$(C_R^{x,y})_y \leftarrow$ solve h_{C_R} using an iterative solver calling `local_apply_h_c` at x

$(C_L^{x,y})_y \leftarrow$ solve h_{C_L} using an iterative solver calling `local_apply_h_c` at $x - 1$

for $y \in \{0, \dots, n_y\}$ **do**

$|\psi(A_y)\rangle\rangle, \epsilon_{trunc,y} \leftarrow \{A_C^{x,y}, C_R^{x,y}, C_L^{x,y}\}$ following (33) and (35)

$\epsilon_{gauge} \leftarrow \max\{\epsilon_{gauge,y}\}$

$(L_{x,y})_{x,y}, (R_{x,y})_{x,y} \leftarrow$ update environments from $\{(|\psi(A_y)\rangle\rangle_y, M\}$ calling `environment_terms`
